JPhys Photonics

Multi-parametric photoacoustic elastomicroscopy: quantitative elasticity mapping and microstructural analysis for early-stage hepatic fibrosis detection

To cite this article: Weiran Pang *et al* 2025 *J. Phys. Photonics* **7** 045038

IOP Publishing J. Phys. Photonics 7 (2025) 045038 https://doi.org/10.1088/2515-7647/ae0541

Journal of Physics: Photonics

OPEN ACCESS

RECEIVED
16 July 2025

REVISED
18 August 2025

ACCEPTED FOR PUBLICATION
9 September 2025

PUBLISHED
15 October 2025

PAPER

Multi-parametric photoacoustic elastomicroscopy: quantitative elasticity mapping and microstructural analysis for early-stage hepatic fibrosis detection

Weiran Pang[1,2], **Qi Zhou**[2], **Yang Qiu**[2], **Haofan Huang**[1], **Jiali Chen**[2], **Tianting Zhong**[1], **Yingying Zhou**[4,*], **Liming Nie**[2,*] **and Puxiang Lai**[1,3,*]

[1] Department of Biomedical Engineering, The Hong Kong Polytechnic University, Hong Kong Special Administrative Region of China, People's Republic of China
[2] Medical Research Institute, Guangdong Provincial People's Hospital (Guangdong Academy of Medical Sciences), Southern Medical University, Guangzhou 510080, People's Republic of China
[3] Joint Research Centre for Biosensing and Precision Theranostics, The Hong Kong Polytechnic University, Hong Kong Special Administrative Region of China, People's Republic of China
[4] College of Professional and Continuing Education, The Hong Kong Polytechnic University, Hong Kong Special Administrative Region of China, People's Republic of China
[*] Authors to whom any correspondence should be addressed.

E-mail: ying2zhou@cpce-polyu.edu.hk, **nieliming@gdph.org.cn** and **puxiang.lai@polyu.edu.hk**

Keywords: photoacoustic elastomicroscopy (PAEM), liver fibrosis, tissue stiffness, time of flight (ToF), elastic sensing and measurement, tumor margins, multi-parametric evaluation

Supplementary material for this article is available online

Abstract

Early detection of hepatic fibrosis remains a critical unmet need due to the limited sensitivity of conventional elastography in capturing microstructural and biomechanical changes. In this study, we developed photoacoustic elastomicroscopy (PAEM), a multi-parametric imaging platform that synergizes high-resolution photoacoustic microscopy with time-of-flight (ToF)-based elastography to quantitatively map tissue stiffness and visualize fibrotic microarchitecture. Validated using PDMS phantoms and a drug-induced murine fibrosis model, PAEM can detect early-stage fibrosis through microstructural biomarkers—pseudo-lobule formation and crevice-area expansion, with a relatively high area under the curve (AUC) > 0.91. However, architectural ambiguity in advanced fibrotic stages gradually reduces PAEM's diagnostic accuracy, necessitating complementary reliance on ToF-based measurements for auxiliary staging. In our results, ToF-based elasticity biomarkers revealed progressive stiffness increases with a significant velocity increase of 3.7% in 1-week fibrosis. Furthermore, experimental PAEM outperformed shear wave elastography (SWE) in early-stage sensitivity by identifying significant stiffness changes, quantitatively 7-fold greater velocity differential sensitivity than SWE (5.39% vs. 0.77% change), between healthy and 3-week fibrotic liver tissue. All-stage fibrosis exhibited a considerable stiffness rise (AUC > 0.95), correlating strongly with histopathological severity and serum examination. By integrating structural and mechanical biomarkers, PAEM offers a translational tool for early diagnosis, longitudinal monitoring, and staging of hepatic fibrosis, which can potentially be extended for wider applications in tumor margin delineation and other fibrotic pathologies in soft tissue.

1. Introduction

Tissue elasticity has emerged as a crucial biomarker for early disease diagnosis, with pathological stiffness often preceding macroscopic structural changes in conditions such as cancer and fibrosis. While palpation historically provided the first clinical insights into tissue mechanics, its subjective nature and lack of quantification [1–3] spurred the development of elastography techniques, including magnetic resonance elastography (MRE), ultrasound elastography (USE), and optical coherence elastography (OCE). Among these, MRE enables noninvasive stiffness mapping but suffers from limited spatial resolutions (∼1 mm), hindering its ability to detect microstructural collagen deposition in early liver fibrosis [4, 5]. Furthermore, the substantial capital expenditure and per-procedure operational costs have constrained its clinical adoption compared to USE. Ultrasound-based methods like shear wave elastography (SWE) and transient elastography offer real-time quantitative imaging but also face limited resolution. Evidence indicates that both MRE and SWE, when optimized with appropriate diagnostic thresholds, achieve sensitivity around 90% for detecting advanced-stage fibrosis [6], however lose accuracy in early-stage fibrosis and obese patients, where stiffness gradients are subtle and heterogeneous [7]. Conversely, OCE is achieves micron-scale resolution but is restricted to superficial tissue regions such as ocular tissues and skin due to optical scattering [8, 9]. Investigators quantified shear wave OCE sensitivity by assessing velocity variance in repeated phantom measurements, demonstrating reliable detection of shear wave speed (SWE) changes below 4% with statistical significance [10, 11]. Atomic force microscopy (AFM) provides nanoscale mechanical characterization but remains invasive and incompatible with in-vivo applications [12]. These limitations underscore the unmet needs for a modality combining deep-tissue penetration, microscopic resolution, and multi-parametric sensitivity to both structural and mechanical biomarkers.

Liver fibrosis, a progressive condition, characterized by the excessive accumulation of extracellular matrix proteins, is driven by chronic liver injury due to various etiologies such as viral hepatitis, alcohol abuse, and non-alcoholic fatty liver diseases [13], exemplifies this diagnostic challenge. Current staging relies on invasive biopsy or single-parametric imaging tools like SWE and MRE, which struggle to resolve early microarchitectural changes such as pseudo-lobule formation and diffusion collagen deposition [14–16]. Pathologically, fibrosis begins with localized extracellular matrix remodeling that subtly alters tissue viscoelasticity—a signature undetectable by conventional elastography until cirrhosis develops [16]. Early intervention during this reversible phase could prevent progression to end-stage liver disease, yet no clinically viable method currently bridges the gap between cellular-scale biomechanics and organ-level stiffness mapping.

Photoacoustic (PA) imaging, a modality combining optical excitation and ultrasound emission, has been employed in diverse biomedical applications over the past two decades [17–19]. As an emerging variant based on the PA effect, PA elastography (PAE) utilizes laser-induced ultrasound signals to encode both optical absorption and mechanical properties [20]. Current PAE implementations can be categorized into three paradigms: stress-strain analysis, where external mechanical loading is applied to measure tissue deformation via PA tracking [21–23]; phase/frequency-domain methods, correlating viscoelastic properties with phase delays or resonance frequency shifts in PA waveforms [24, 25]; time-of-flight (ToF) or time-domain techniques, exploiting sound speed variations in tissues to infer stiffness changes [26, 27]. Stress-strain PAE, exemplified by Hu *et al* [23], quantifies absolute Young's modulus by analyzing displacement fields under controlled compression. While effective for skin and breast tissues, this approach struggles in soft, fluidic organs like the liver due to challenges in achieving uniform stress distribution and avoiding tissue damage [28]. Phase-domain methods, such as Yang *et al*'s elasto-viscography [24] detect stiffness differences by measuring the laser-induced thermoelastic phase delays. Although sensitive to microscale viscoelasticity, these methods require complex signal processing and high-frequency transducers, limiting their depth penetration in turbid tissues [25]. Time-based PAE, as demonstrated by Yuan *et al* [26] offers non-contact elasticity sensing by analyzing the ultrasound propagation delays. However, existing implementations lack microscopic resolution (>500 μm) and fail to integrate structural biomarkers (e.g. collagen architecture) with mechanical readouts—a critical gap for detecting early fibrosis where microstructural remodeling precedes bulk stiffness changes [29, 30]. Furthermore, most PAE systems focus on single-parametric elasticity metrics, neglecting the synergistic diagnostic value of combining mechanical and morphological data. For hepatic applications, these limitations are compounded by the liver's acoustic heterogeneity and the sub-millimeter scale of early fibrotic features (*e.g.* sinusoidal capillarization, sub-500 μm pseudo-lobules) [29], which conventional PAE cannot resolve.

In this study, we introduce PA elastomicroscopy (PAEM), a high-resolution platform integrating ToF-based elasticity mapping with microstructural analysis for multi-parametric liver fibrosis assessment. By synergizing PA microscopy (PAM)'s optical resolution (∼7.5 μm) with acoustic wave propagation physics, PAEM simultaneously quantifies stiffness gradients and visualizes fibrotic microarchitecture in a label-free manner. We validate PAEM's precision using phantoms with tunable mechanical properties and demonstrate its biomedical utility in a longitudinal murine fibrosis model. Our results establish PAEM's superiority over SWE in early-stage detection, enabled by correlating crevice-area expansion (structural biomarker) with ToF-derived stiffness progression (mechanical biomarker). This dual-parametric approach addresses the critical limitations of single-modality elastography, positioning PAEM as a translational tool for fibrosis staging, tumor margin delineation, and therapeutic monitoring.

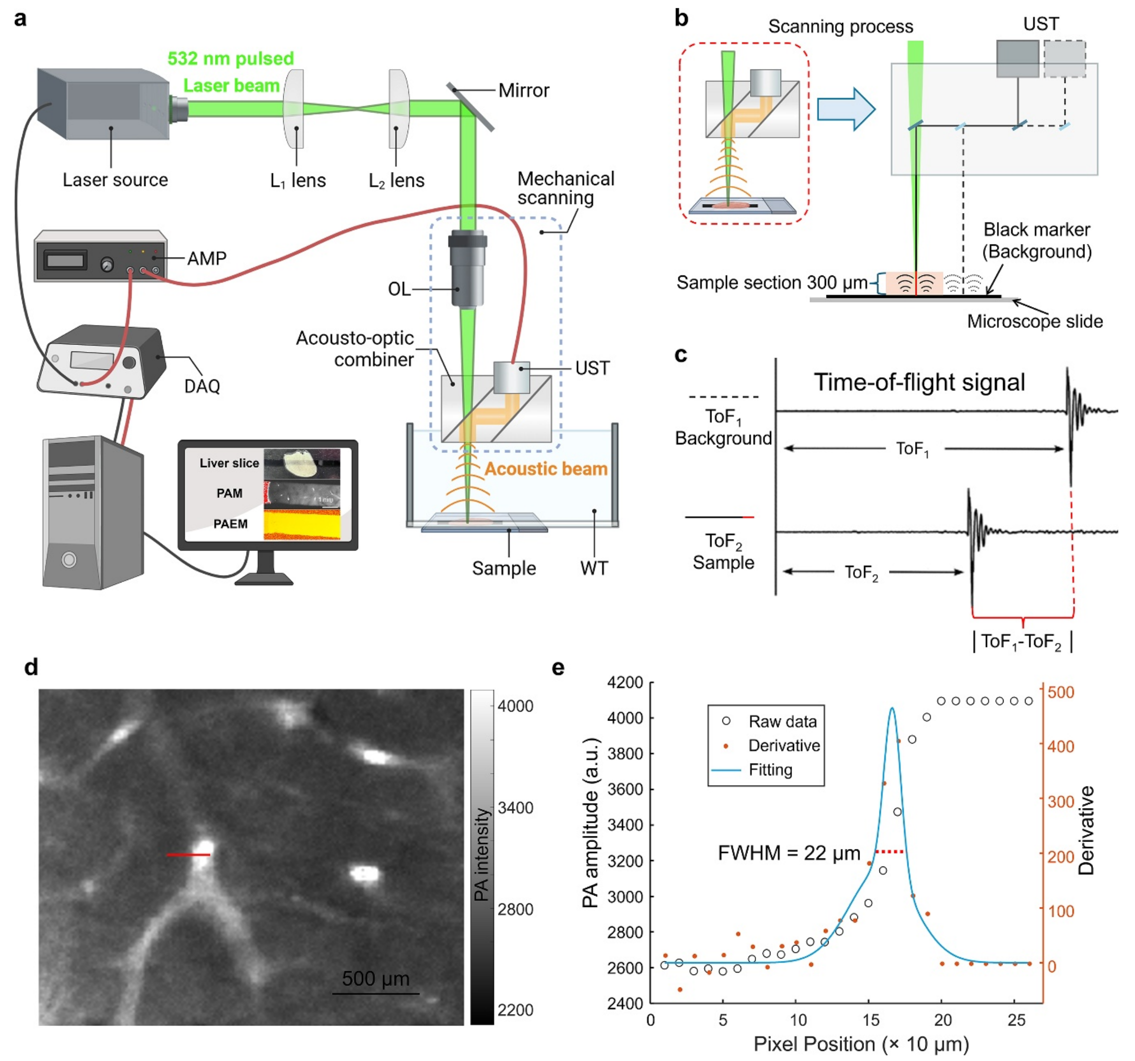

Figure 1. PAEM system and ToF-based elasticity measurement principle. (a) Schematic diagram of the PAEM setup. AMP: Amplifier, DAQ: Data acquisition (sampling rate 500 MS s^{-1}), OL: Objective lens, UST: Ultrasonic transducer (central frequency 50 MHz, bandwidth 60%), WT: Water tank. (b) Representative B-scan of a liver section, highlighting ToF differences between the background (black marker, ToF$_1$) and sample section (ToF$_2$). (c) Calculation of ΔToF, reflecting ultrasound velocity variations due to sample stiffness. (d) Liver PA image with massive vascular structure. (e) The estimated small-vessel resolvability.

2. Results and discussion

2.1. ToF-based PAEM measurement

The PAEM system (figure 1(a)) leveraged ToF differences to quantify relative stiffness variations (ultrasound propagation speed) in liver tissues. When pulsed laser irradiates the liver sample, the black marker background absorbs the light and generates ultrasonic signals via the thermoelastic effect; the weak absorption of the liver section is negligible in comparison. The ultrasound propagates through the liver slide and travels back to the ultrasound transducer, with the propagation time defined as ToF. However, due to variations in stiffness within the liver samples, the ultrasound velocity differs, leading to variations in propagation time within the tissue and, consequently, differences in arrival time at the ultrasound transducer. A single B-scan should ideally encompass both the signal cover with the liver section and the background region without liver tissue (figure 1(b)). To quantify the differences, we calculate ToF$_1$ in the background region and ToF$_2$ in the sample section, and the difference between them ($\Delta\text{ToF} = |\text{ToF}_1\text{–ToF}_2|$) serves as a proxy for stiffness, with shorter ToF indicating higher sound speed and greater tissue rigidity (figure 1(c)). This approach offers a high resolution as traditional optical-resolution PAM ($\sim$7.5 μm lateral system resolution, figure S1). A raw PA response perpendicular to major blood vessels was extracted (red line in figure 1(d)). Using the edge spread function method, the first-order derivative of the signal was computed and subsequently subjected to Gaussian fitting. The full width at half maximum of the fitted curve was determined as the small-vessel resolvability in the liver sections, yielding a value of 22 μm

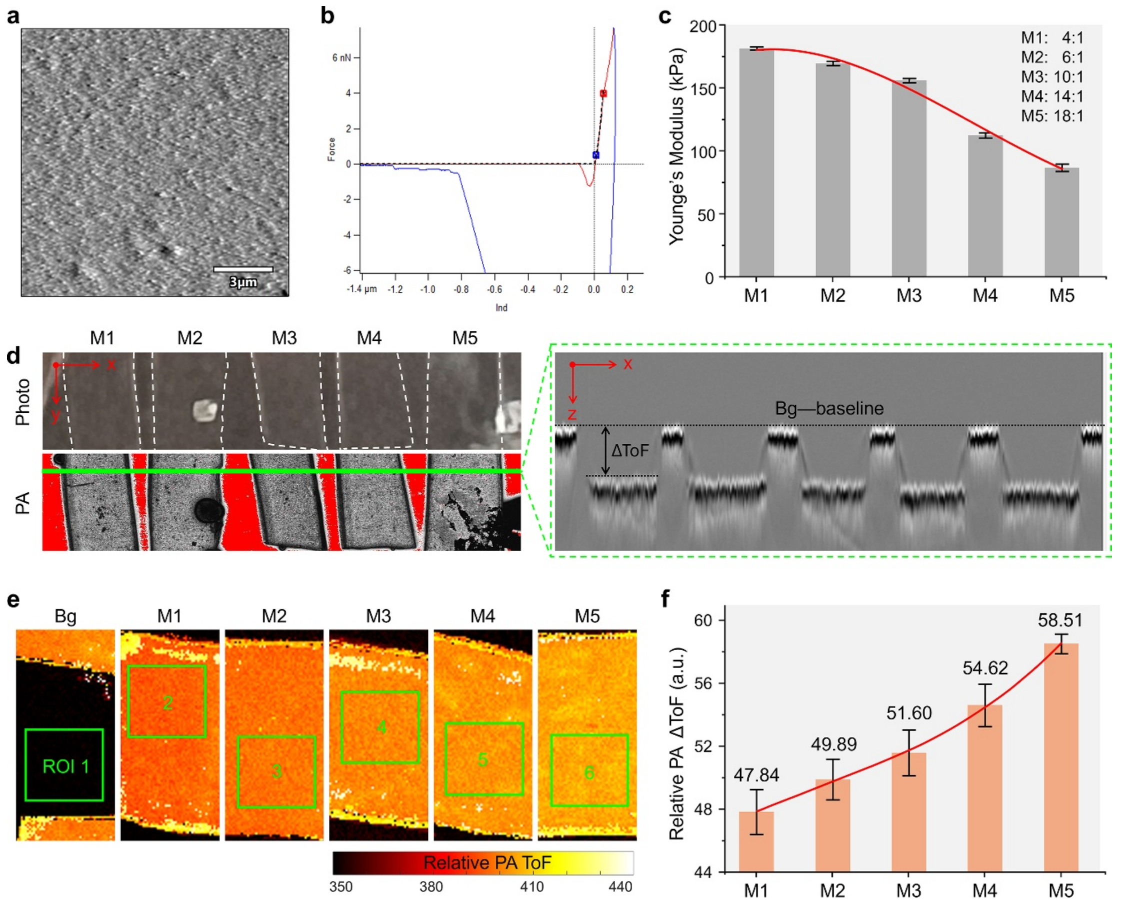

Figure 2. PAEM elasticity validation using PDMS phantoms with tunable stiffness. (a) AFM surface morphology of a PDMS thin film, showing uniform topography. (b) Representative AFM force-displacement curve for PDMS elasticity quantification. Young's modulus was calculated using the Hertz contact model (dashed line: fitted curve). (c) Young's modulus of PDMS films decreases with increasing base-to-curing agent ratios (M1-M5). (d) PA and ToF images of PDMS films. The PA image represents a maximum intensity projection (MIP) in 2D, while the ToF signal corresponds to the time-resolved PA waveform along the *z*-axis at the position marked by the green line in the PA image. Bg: Background. (e) PAEM-derived ToF elasticity maps, color-coded to reflect stiffness variations. ROI: region of interest. (f) ΔToF increases with softer PDMS formulations, inversely correlating with Young's modulus.

(figure 1(e))—sufficient for capillary-scale visualization. So, PAEM provides multi-parametric capabilities of simultaneous cellular-scale structure visualizing and organ-level stiffness mapping.

2.2. PAEM elasticity validation using PDMS films

To assess the capability of PAEM in measuring elasticity, validation experiments with AFM and PAEM measurements were conducted using PDMS thin films with varying compositions. We employed PDMS materials spanning five distinct stiffness gradients. These were fabricated by varying the base-to-curing agent weight ratio (M1–M5 ratios: 4:1, 6:1, 10:1, 14:1, and 18:1, respectively) and cast into 300 μm-thick films for phantom experiments. Figure 2(a) presents the surface morphology of a PDMS thin film, showing a relatively smooth texture, which ensures uniformity in elasticity measurements. AFM force-displacement curves were obtained (figure 2(b)), and the compressive Young's modulus was calculated using the Hertz contact model. The correlation between measured Young's modulus and PDMS composition is depicted in figure 2(c), showing a decreasing trend in stiffness as the PDMS ratio increases. This trend aligns with known material properties, where a higher ratio results in a softer, less cross-linked elastomer [31].

PA image of the PDMS thin films (figure 2(d)) visualized the internal structural features. By extracting the depth profile (*x*–*z* plane) along the green line drawn on the PA image, we observe that the ToF at the film location is significantly greater than the ToF baseline in the background (green box in figure 2(d)). This occurs because: the crosslinking reaction of PDMS affects its mechanical and acoustic properties, including the internal speed of sound within the material. The decrease in the crosslink density results in the decrease in the hypersonic sound velocity [32]. PDMS polymers or elastomers typically exhibit a natural sound speed of approximately 1000–1200 m s^{-1}, which is significantly lower than the 1500 m s^{-1} speed of sound in water. As a result, the measured ToF in PDMS is greater than that in the background. Furthermore, as the PDMS ratio increases, the material becomes softer, leading to a slower sound propagation speed within the films. The ToF elasticity maps were generated by identifying the temporal positions corresponding to the average maximum amplitude along the depth (z-direction) within the PA matrix, which were used to provide quantitative elasticity mapping. Within each film, three spatially non-overlapping regions of interest (ROIs) were randomly selected for ΔToF calculation, with three additional ROIs similarly chosen in the background region. As illustrated in figure 2(e), all ROIs were positioned in areas exhibiting relative homogeneity. Calculated as $\Delta\text{ToF} = |\text{ToF}_{\text{background}} — \text{ToF}_{\text{PDMS}}|$, ΔToF increased progressively from the stiffest (M1) to the softest (M5) PDMS samples (figure 2(f)). As known, the ΔToF is inversely proportional to the ultrasound propagation speed in PDMS films; this implies that it is also inversely proportional to Young's modulus. This PA-ToF measurements trend shows strong agreement with the measured Young's modulus data in figure 2(c), confirming the reliability of this method for elasticity assessment in biological tissues.

2.3. PAEM imaging of liver fibrosis microstructure

The aim of this study was to assess the degree of liver fibrosis based on the comprehensive evaluation of these parameters and to investigate whether the proposed ToF-based PAEM could serve as an effective tool for sensing and diagnosing liver fibrosis and other elasticity-related diseases. As shown in figure 3, the diagram illustrates the integration of PAEM with histopathological and serum biomarker analyses in a CCl_4-induced liver fibrosis mouse model. We established a drug-induced liver fibrosis mouse model by regularly administering a mixture of CCl_4 and olive oil via intraperitoneal injection. CCl_4-induced liver fibrosis predominantly triggers cellular injury and necrosis in the central venous region of hepatic lobules, promoting the differentiation of myofibroblast-like cells. These changes subsequently disrupt hepatic microstructure and compromise tissue elasticity [29]. During animal modeling, various parameters were recorded at different time points, including body weight, liver wet weight, serum liver function markers, and liver histology.

The limited spatial resolution of SWE (commonly used in clinic) precludes its ability to resolve microstructural features, as it primarily infers Young's modulus elasticity values through measurements of shear wave speed (SWS) within tissues. Early-stage liver fibrosis is characterized by predominant microstructural remodeling rather than quantifiable elasticity alterations. This fundamental pathological progression renders SWE insensitive to incipient fibrotic changes—both structurally and in terms of measurable elasticity variations—during initial disease phases. Our experimental measurements of liver stiffness via SWE in both healthy controls and 3-week fibrotic mice quantitatively confirmed this pattern (healthy: SWS 1.5954 ± 0.0581 m s^{-1} vs fibrotic: SWS 1.6077 ± 0.0566 m s^{-1}, $p = 0.62 \gg 0.05$). As demonstrated in figure S2, SWE revealed no significant differences in tissue elasticity; however, histopathological analysis identified substantial collagen fiber deposition. Enhancing early diagnostic sensitivity and preventing irreversible late-stage hepatic damage represent critical objectives in chronic liver disease management. This underscores an urgent need to develop noninvasive diagnostic adjuncts capable of detecting incipient fibrosis and enabling longitudinal monitoring of disease progression.

To solve this problem, we performed PAEM imaging of the liver, key stages include: (1) PAEM imaging of 300 μm thick liver sections to capture structural changes (e.g. pseudo-lobule formation and crevices area), (2) elasticity mapping via ToF-based measurements and clear margin delineation, and (3) correlation of PAEM-derived stiffness and microstructural metrics with histology (Masson's trichrome staining) and serum liver function markers alanine aminotransferase/aspartate aminotransferase (ALT/AST). This multi-parametric approach enables comprehensive detection of early fibrosis progression while demonstrating strong correlation with established diagnostic standards. PAEM's unique capacity to integrate structural, biomechanical, and biochemical data offers complementary value to conventional methods, highlighting its potential for non-invasive longitudinal monitoring of hepatic fibrosis. This synergistic capability facilitates more timely diagnosis and precise staged management of fibrosis progression.

Physiological results show that, as fibrosis worsens, the liver surface exhibits an uneven, granular texture (figures S3(a) and (b)), and Masson's trichrome staining reveals an increase in fibrous collagen (blue staining), which divides the hexagonal hepatic lobules into multiple small, irregular pseudo-lobules (figure S3(c)). Although fibrotic mice display significantly lower body weights compared to normal controls, the fibrotic liver becomes enlarged in later stages (figure S4). Elevated serum ALT and AST levels further indicate hepatic inflammation and injury (figure S5). Nevertheless, these parameters demonstrate neither consistent progression patterns nor well-defined thresholds for fibrosis grading.

In PAEM imaging, 300 μm thick slices were carefully laid on glass slides marked with a black marker and put on the imaging planes. It is crucial that the scanning area, encompasses both the liver slice and the adjacent marker region (lacking liver tissue) to facilitate subsequent ΔToF calculations. As illustrated in figure 4(a), the PA structural images reveal the formation of additional pseudo-lobules. We employed an algorithm to extract the skeleton of the pseudo-lobule crevices—hereafter referred to as 'Crevices'—and

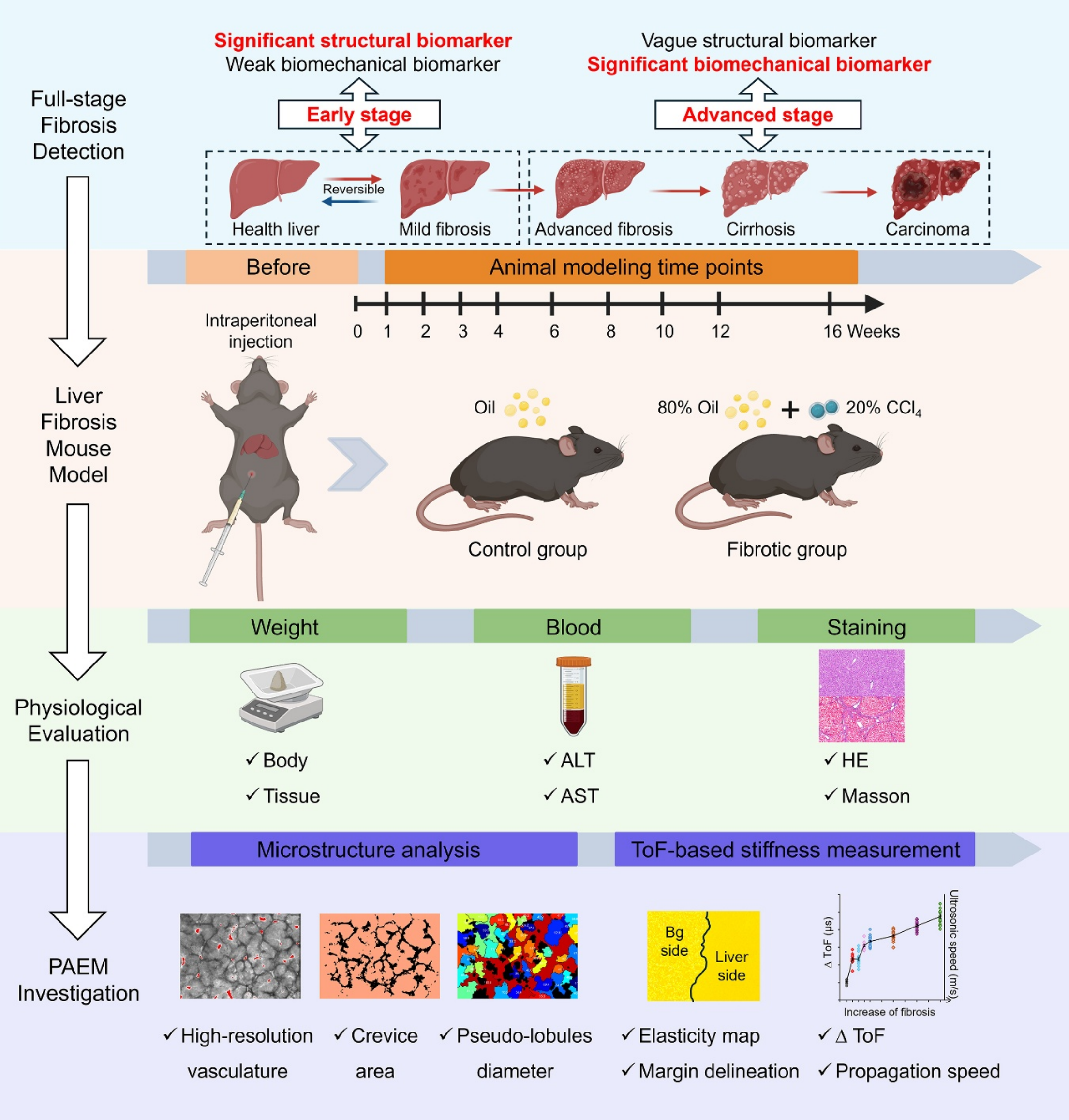

Figure 3. Schematic workflow of multi-parametric PAEM imaging and sensing for mouse liver fibrosis assessment. Using CCl_4-induced hepatic fibrosis models (stages: 1–16 weeks), we implemented a multi-parameter diagnostic strategy. During early stages (1–4 weeks), high-resolution PAEM structural analysis was prioritized to detect microarchitectural alterations—which precede measurable biomechanical changes—as primary biomarkers. In advanced stages (>4 weeks), where tissue stiffening supersedes structural evolution, ToF-based elasticity measurements quantitatively tracked mechanical property progression. Fibrosis staging throughout the disease continuum was validated against histopathological grading and physiological parameters, demonstrating the significant advantage of our multiparametric approach for comprehensive fibrosis assessment.

calculated their area and relative proportion, observing a relatively linear increase (figure 4(b)), which is in line with the collagen proportionate area (CPA) calculations of Masson's staining (figures 4(e) and (f)). These Crevices partition the liver lobules into irregularly shaped pseudo-lobules. An algorithm was further used to delineate these irregular regions, assign them random color codes, and compute their maximum diameters. The most frequently observed diameter was 560.6 μm; as fibrosis progressed, the overall lobule diameters gradually decreased while the proportion of regions with a 560.6 μm diameter increased (figure 4(c)). Finally, we analyzed the distribution of these diameters based on a normal distribution. The fitted curves indicated that early-stage liver fibrosis (weeks 1–4) could be distinctly differentiated, whereas advanced fibrosis (weeks 4–16) exhibited no clear pattern or significant differences (figure 4(d)). These results indicate that relying solely on changes in liver structure, such as the area of Crevices and diameter statistics, allows for the detection and distinguish of early-stage fibrosis. However, advanced liver fibrosis obscured structural patterns, necessitating complementary elasticity metrics for accurate staging.

2.4. ToF-based PA sensing of liver stiffness

We extracted the mean ToF peak values along the A-line direction from the 3D matrix of the PA signal, forming a new image matrix that represents the elasticity map. For each liver sample, ToF values were

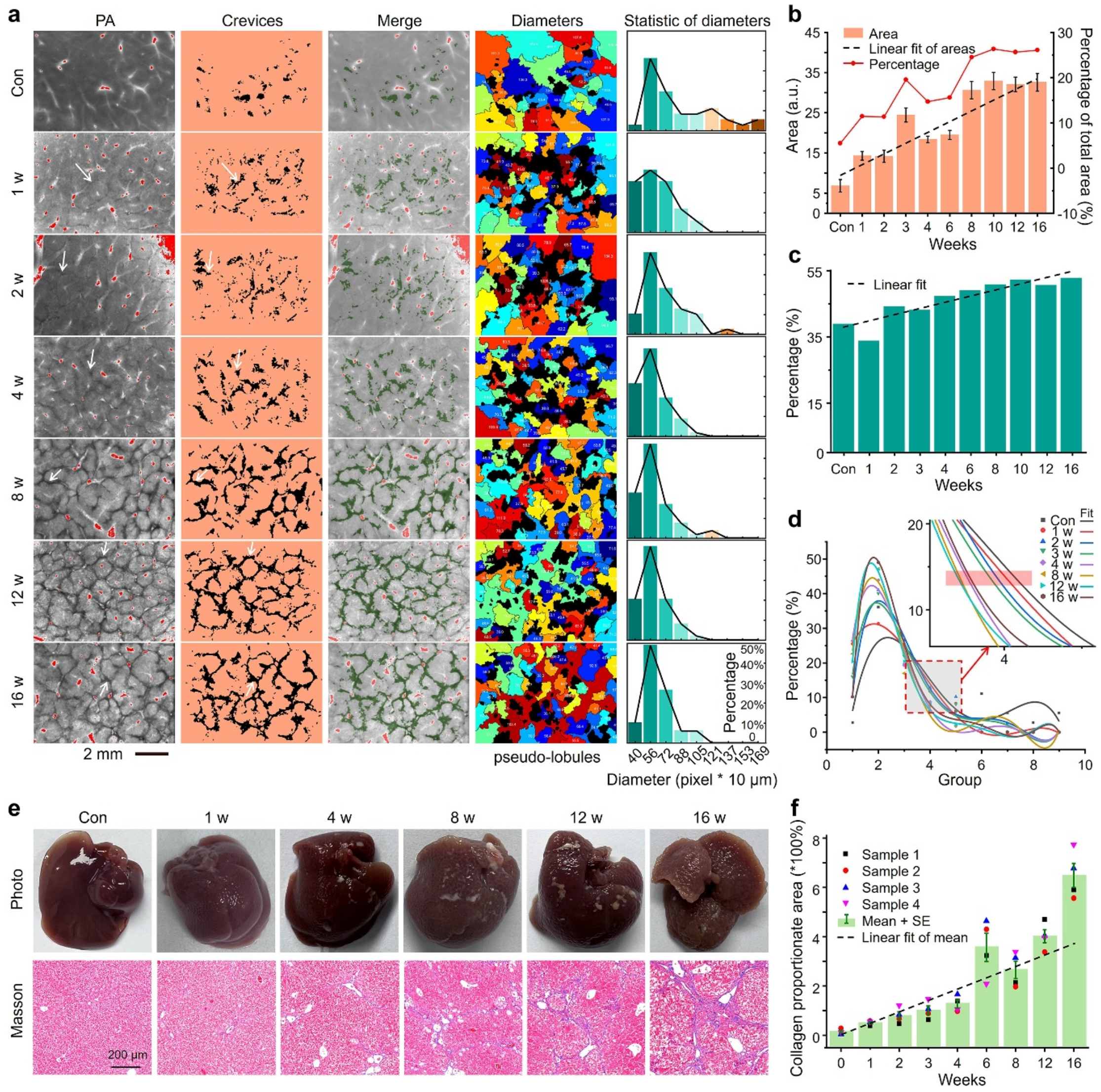

Figure 4. PAEM structural imaging reveals microarchitectural remodeling in fibrotic liver. (a) PAEM structural images of liver sections at progressive fibrosis stages (control and weeks 1–16). Pseudo-lobule formation (color-coded regions) and crevice expansion (white arrows) are evident as fibrosis advances. (b) Quantification of crevice area proportion shows a linear increase during mild to moderate fibrosis (weeks 1–6), plateauing in advanced stages. (c) Histogram of pseudo-lobule diameters identifies a dominant size (560.6 μm), with reduced mean diameters in early fibrosis (dashed line). (d) Normal distribution fitting of diameters highlights distinct clustering in early stages (control and weeks 1–4) versus overlapping distributions in advanced fibrosis (weeks 4–16). (e) Liver surface texture and Masson's trichrome staining. (f) Quantification of CPA. Each group included four samples, and the results showed a gradual increase in collagen fiber area percentage, indicating progressive fibrosis.

randomly selected from both the liver side and the background side ($n = 3$), and the ΔToF was calculated as the difference between $\text{ToF}_{\text{backgroud}}$ and $\text{ToF}_{\text{liver}}$. Since the ultrasound longitudinal wave speed (LWS) within the liver tissue is proportional to liver components and stiffness (collagen deposition), and the speed is directly related to ΔToF, it is reasonable to assume that ΔToF correlates positively with liver stiffness. Thus, the changes in stiffness were reflected by the variation in ΔToF values. The sample size for each week was $n \geqslant 11$. One-way analysis of variance (ANOVA) showed that the data followed a normal distribution.

Assuming the LWS in water to be 1500 m s^{-1} ($\nu_{\text{background}}$), we calculated that the LWS in normal liver tissue (ν_{liver}) was approximately 1539 m s^{-1}, which is consistent with previously reported values for healthy liver tissue [33]. As seen (figure 5(a)), early stages (weeks 1–2) showed modest ΔToF increases (0.012 ± 0.004 μs, ν_{liver} ~1596 m s^{-1}), which may be attributed to protective hepatic mechanisms and immune responses that counteract fibrosis development during this potentially reversible phase. Significant stiffness changes emerged at week 3 ($\Delta\text{ToF} = 0.015 \pm 0.003$ μs and $\nu_{\text{liver}} = 1622$ m s^{-1}, $p \ll 0.05$). The statistically equivalent SWE velocities (0.0123 m s^{-1} increase) align with known limitations in early fibrosis detection. Conversely, PAEM detected a significant 83 m s^{-1} increase ($1539 \rightarrow 1622$ m s^{-1}) in 3 week fibrotic livers, demonstrating 7-fold greater velocity differential sensitivity than SWE (5.39% vs 0.77% change). Additionally, our methodology detected a significant ΔToF shift within the first week, corresponding to an

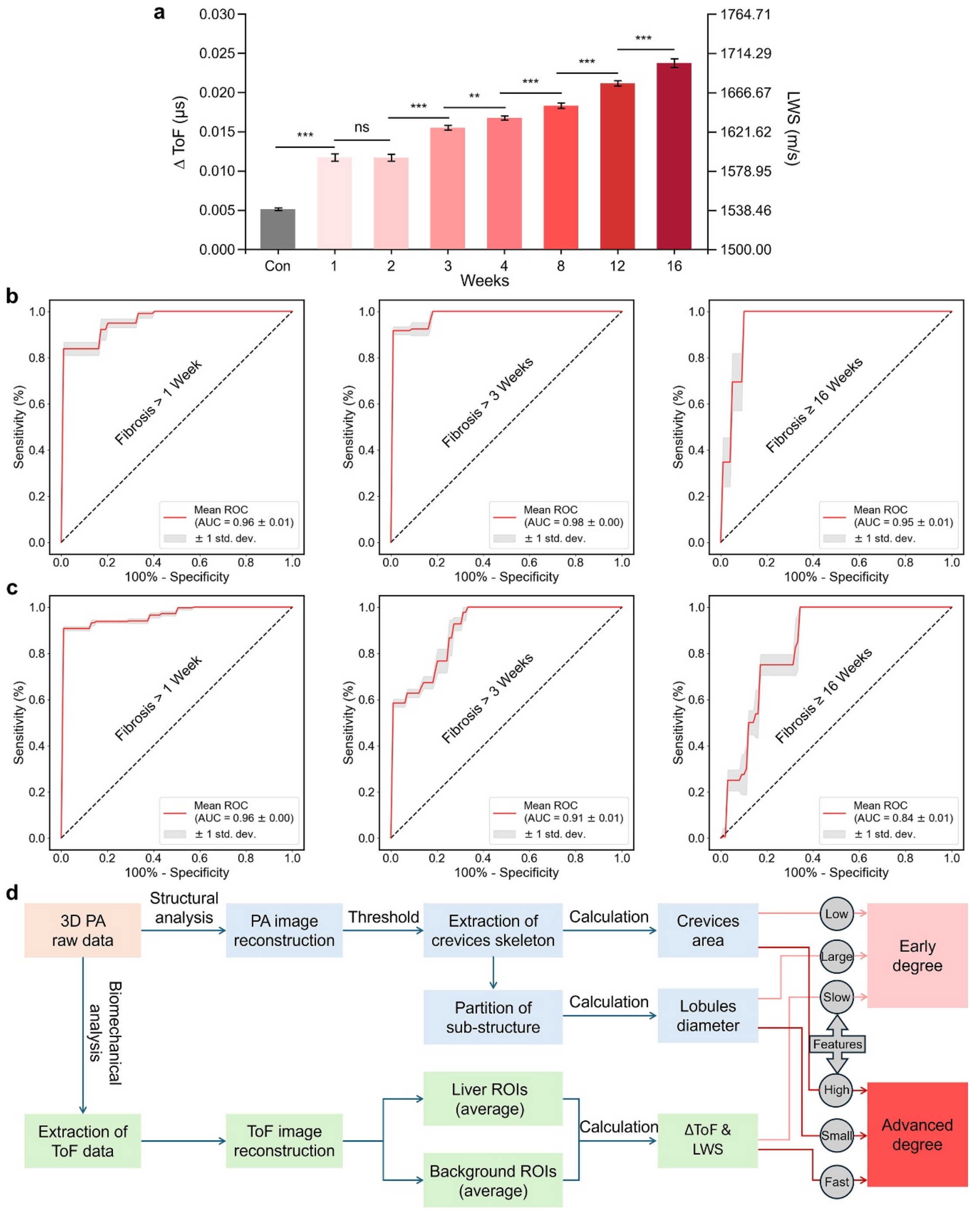

Figure 5. ToF-based PAEM elastic sensing tracks progressive liver stiffening during fibrosis. (a) Longitudinal changes in ΔToF and LWS across fibrosis stages. Statistical comparisons confirm distinct elasticity differences between different fibrosis stages. (b) Elastic ToF measurements evaluate hepatic fibrosis staging through ROC curve analysis. (c) Structural crevices-area calculations evaluate hepatic fibrosis staging through ROC curve analysis. (d) Combined application of PAEM in staging fibrosis. Early and advanced stages of liver fibrosis can be distinguished through multi-feature classification.

LWS variation of 57 m s^{-1}(from 1539 to 1596 m s^{-1})—representing a 3.7% velocity increase. This quantifiable early-stage alteration demonstrates the superior detection sensitivity of the PAEM approach, indicating significant advantages of our methods over conventional elastography. The ToF-based methodology offers dual capabilities: sensitive incipient fibrosis detection (Stage: 1–3 weeks) and quantitative LWS-based stiffness mapping across all fibrotic phases (Stage: 1–16 weeks). As examined by receiver operating characteristic (ROC) curve, ToF measurements could differentiate between normal, early fibrosis, and advanced fibrosis stages with a high sensitivity and specificity (area under the curve: $AUC > 0.95$, figure 5(b)).

Compared to ROC analysis of structural features, ToF-based measurements demonstrate consistently high diagnostic sensitivity and specificity across all fibrotic stages. In contrast, structural analysis maintained

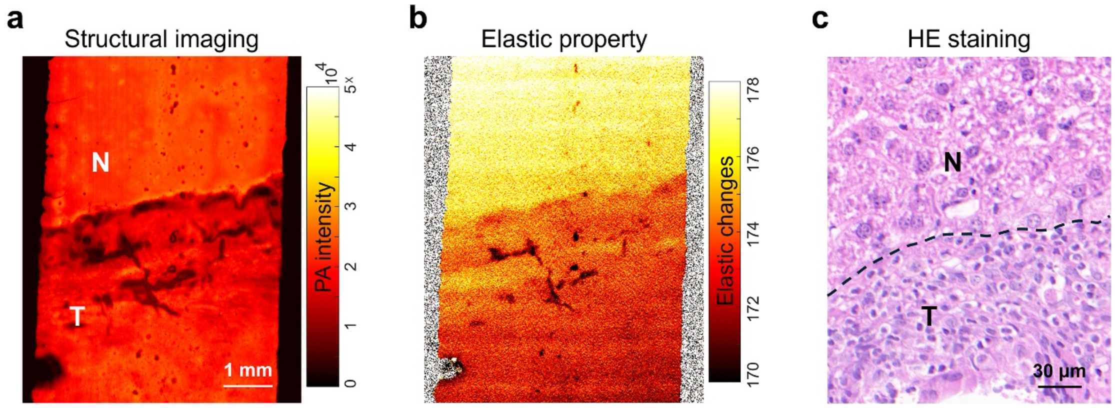

Figure 6. PAEM delineates tumor boundaries through combined structural and elastic imaging. (a) PA structural image of a liver section containing adjacent tumor (T) and normal (N) tissues, revealing irregular tumor margins. (b) PAEM elasticity map demonstrates a progressive stiffness gradient, with elevated rigidity in the tumor core (red-orange) compared to surrounding normal parenchyma (yellow-white). (c) Corresponding H&E staining validates the histopathological boundary (dashed line) between tumor and normal regions.

elevated sensitivity only during earlier phases (figure 5(c)). We therefore conclude that multiparametric integration—encompassing both microarchitectural and biomechanical properties—is essential for comprehensive fibrosis assessment.

In summary, PAEM achieves early diagnosis and therapeutic monitoring through dual complementary pathways feature classification (figure 5(d)):

(1) Microstructural evaluation pathway (Up panel):
  - Raw 3D PA data undergo reconstruction to visualize hepatic architecture
  - Algorithm-driven extraction of fibrosis-induced crevices skeletons partitions the parenchyma into discrete sub-structures
  - Quantitative analysis of two key morphological biomarkers: crevices area (sub-threshold pixels)—reflecting collagen deposition; lobules diameter (colored)—indicating parenchymal remodeling
  - These structural parameters show diagnostic sensitivity primarily in early fibrosis stages (weeks 1–4)

(2) ToF-based stiffness pathway (Down panel):
  - ToF data extracted from the 3D PA matrix are reconstructed into elasticity maps
  - Paired measurements from liver ROIs and background ROIs yield ΔToF values
  - Conversion to ultrasound propagation speed ($\Delta\text{ToF} \rightarrow \nu_{\text{liver}}$) provides direct quantification of tissue stiffness
  - This biomechanical parameter exhibits progressive elevation from week 3 onward, correlating with irreversible fibrotic progression

Critically, the convergence of these orthogonal datasets—structural (spatial) and elastic (mechanical)—creates a diagnostic matrix where early-stage sensitivity (structural) and late-stage specificity (elastic) synergistically enhance detection accuracy. The superimposed regression curves in figure 5(d) demonstrate how integrated parameter analysis resolves diagnostic ambiguities: Structural parameters plateau in advanced fibrosis while elasticity metrics maintain discriminative power, enabling comprehensive staging across the fibrotic continuum. So, multi-feature classification can increase diagnostic accuracy.

2.5. Tumor margin delination via PAEM

If liver fibrosis is not treated early, it can progress to severe hepatocarcinogenesis. The results above demonstrate that ToF-based PAEM is highly sensitive to early-stage liver fibrosis and has capability for monitoring fibrosis progression via sensing of multi-parametric structural and elastic information. This method may further offer benefit of distinguishing hepatocellular carcinoma from adjacent normal tissue. Structural imaging highlighted irregular tumor boundaries (figure 6(a)), while elasticity maps revealed a stiffness gradient increasing toward the tumor core (figure 6(b)). These findings aligned with histopathology (figure 6(c)), demonstrating PAEM's dual capability in resolving both morphological and biomechanical hallmarks of malignancy. Such high-resolution and high-sensitivity elasticity sensing underscores its potentials for precise tumor margin identification and stiffness-guided diagnosis of hepatic malignancies.

3. Conclusion

Early diagnosis of liver fibrosis is crucial for halting disease progression and improving patient outcomes. However, conventional techniques such as biopsy and USE face limitations in sensitivity, resolution, and practicality for longitudinal monitoring. To address these challenges, we developed PAEM, a multi-parametric imaging platform that synergizes high-resolution structural visualization with ToF-based biomechanical sensing. PAEM demonstrated exceptional sensitivity to early fibrotic changes in a CCl4-induced mouse model, detecting microstructural remodeling (e.g. pseudo-lobule formation, crevice expansion) and incremental stiffness increases ($\Delta\mathrm{ToF} = 0.015 \pm 0.003$ μs at week 3, $\nu_{\mathrm{liver}} \approx 1622$ m s^{-1}) that conventional SWE failed to resolve. By integrating high-resolution, high-sensitivity elasticity mapping with histopathological and serum biomarker analyses, PAEM achieved comprehensive fibrosis staging, bridging the gap between microscopic tissue alterations and macroscopic clinical metrics, offering complementary value to conventional methods for non-invasive longitudinal monitoring of hepatic fibrosis.

Notably, PAEM's ability to delineate tumor margins via stiffness gradients underscores its versatility beyond fibrosis, offering potential applications in oncology for boundary definition and treatment planning. Two essential prerequisites must be emphasized for the proposed PAEM methodology: First, sample thickness must be precisely known and spatially uniform, as it serves as a fundamental parameter for LWS calculations. Second, during PAEM detection, non-compressive contact must be maintained to prevent external force-induced deformation, since both mechanical stress and thickness variations constitute significant confounding variables in LWS computation. Future work will focus on enhancing PAEM's imaging depth [34] and real-time processing capabilities to enable in-vivo clinical translation. For example, the capacity for precise tumor core-to-margin demarcation holds significant promise for intraoperative guidance—particularly in defining resection boundaries during cancer surgery. Additionally, extending its utility to other fibrotic diseases (e.g. pulmonary, renal) and incorporating artificial intelligence-driven image analysis [35, 36] could further automate diagnostics and refine staging accuracy.

In summary, PAEM offers a promising approach to elasticity-based diagnostics by integrating the high resolution of PAM with the functional assessment capabilities of elastography. Its capacity for high-resolution, high-sensitivity, multi-parametric tissue evaluation positions PAEM as a powerful tool for precision medicine, with broad applicability in early disease detection, therapeutic monitoring, and mechanistic studies of fibrosis and malignancy.

4. Methods and materials

4.1. PAEM system design

PAEM is a imaging modality that combines the principles of PA imaging and elastography, which is an adaptation of the classical PAM system [37]. The PAEM system (figure 1(a)) is a custom-built platform integrating pulsed laser excitation, high-resolution acoustic detection, and precision scanning for simultaneous microstructural and elastography imaging. A Q-switched Nd:YAG laser (532 nm wavelength, 1 kHz repetition rate) serves as the light source, generating pulsed illumination with a single-pulse energy of 500 nJ (0.5 mW average power). The laser beam is expanded using a 4 f optical system (L_1 and L_2 lens, 5×) to achieve uniform illumination. The expanded beam is reflected by a dichroic mirror and focused through an objective lens (NA = 0.13, working distance = 50 mm) onto the sample via a custom acousto-optic coupling module. This module features dual reflective planes to align the optical excitation path with the acoustic detection axis, minimizing signal loss.

PA signals generated by thermoelastic expansion are focused by a spherical acoustic lens in the front edge of the acousto-optic coupling module (the edge to focus is about 5 mm) and detected using a plane UST (Olympus, V214-BC-RM, 50 MHz central frequency, 60% bandwidth, Japan). Signals are amplified by a 40 dB receiver (Inno Laser, China) and digitized at 500 MS s^{-1} (Alazar Tech, ATS9352). The propagation time (ToF) of ultrasound waves through the sample is determined from the time delay between the laser pulse trigger and the peak amplitude of the PA signal.

4.2. Phantom preparation

Five polydimethylsiloxane (PDMS, Sylgard 184, Dow Inc., Midland, MI, USA) phantoms mimicking liver stiffness gradients were fabricated by varying the base-to-curing agent ratios (Weight/w): M1 (4:1), M2 (6:1), M3 (10:1), M4 (14:1), and M5 (18:1). These mixtures were stirred at 200 rpm for 15 min using a magnetic stirrer to ensure a homogeneous mixture. Then, the mixture was left to stand at 4 °C for 2 h before being cast into pre-designed rectangular molds (grooves dimensions: width 10 mm × length 50 mm × thickness 300 μm). Finally, the samples were placed in a vacuum chamber and cured at room temperature for 48 h to achieve complete crosslinking, which different stiffness films could be obtained.

4.3. Animal models and fibrosis induction

All procedures followed the National Institutes of Health Guidelines for the Care and Use of Laboratory Animals (China) and were approved by Guangdong Provincial People's Hospital (No. KY2023-1184-01). Healthy C57BL/6 mice (7 weeks old, 18–21 g, half male and half female) were purchased from the Laboratory Animal Center of Guangdong Province (China). We included about 120 mice in this study with 8 excluded due to acute hepatitis mortality. All mice were used to the typical laboratory conditions of humidity (55%), temperature (22.5 °C ± 0.5 °C), 12-hour light/dark cycle, and full access to food and water. In these mice, different stages (weeks 1–16; $n \geqslant 5$) of liver fibrosis were induced by intraperitoneal injection of a 20% carbon tetrachloride (CCl_4) solution (CCl_4, Macklin; 1.5 ml kg^{-1}, dissolved in olive oil at a 4:1 (Volume/v) ratio) three times per week for 1, 2, 3, 4, 6, 8, 12, and 16 weeks, respectively. Control mice were injected with olive oil (1.5 ml kg^{-1}) at the same points. These mice were evaluated 48 h after their last CCl_4 injection to ensure the acute effects of CCl_4 did not affect the measurements and were used to assess the accuracy of 2D SWE and PAEM in staging liver fibrosis. Then they were humanely killed with histologic and serum analyses after imaging.

4.4. Imaging protocol

SWE: Animals were anesthetized with 1% VOL isoflurane, gas flow rate of 1 cm^3 s^{-1}. All mice underwent SWE examinations at a frequency of 18 MHz using Canon Aplio i900 Ultrasound System (Canon Medical System, Japan), equipped with a i18LX5 plane probe. The imaging depth was fixed at 3 cm, and the circle ROI diameter was set to 3 mm. The 2D SWE image was shown as a color-coded signal overlaying with the B-mode image. 13 ROIs were performed to determine the liver stiffness measurements (LSM) values. The color-bar of the SWE image ranged from 0 to 85 kPa.

PAEM imaging: Fresh liver sections (300 μm thickness) are adhered to glass slides pre-marked with a 4 mm-wide black waterproof marker line. A thin layer of tissue preservation solution is applied to minimize dehydration. These samples are covered with plastic wrap stretched taut over a water tank holder, forming a sealed chamber with minimal water volume (<10 ml) to avoid pressure-induced tissue deformation. The wrap contacts the sample without compression, preserving native stiffness. A motorized X-Y stage (X: Voice Coil Motor, SMAC Corporation, USA; Y: Stepper Motor, GMT Global Inc., Taiwan) scans the sample with 10 μm step resolution, enabling high-resolution elasticity matrix acquisition across multiple axial planes. The scanning head is fully submerged in a water chamber to ensure acoustic coupling. Each 10 mm × 10 mm field of view is acquired at a B-scan rate of 5 Hz, requiring 3.3 min per full C-scan. A-line signals are sampled at 512 points per scan line. Raw PA signals are processed using a custom algorithm in MATLAB (MathWorks) to reconstruct MIP maps. ToF elasticity were computed as $\Delta\mathrm{ToF} = \mathrm{ToF}_{\mathrm{background}}$—$\mathrm{ToF}_{\mathrm{liver}}$, which reflects the variation in sound speed across different liver regions. This relationship can be further expressed as $\Delta\mathrm{ToF} = d/\nu_{\mathrm{background}}$—$d/\nu_{\mathrm{liver}}$, where d presents the sample thickness. Accordingly, assuming an ideal sound speed of 1500 m s^{-1} in water ($\nu_{\mathrm{background}}$), the acoustic velocities within different liver lobes can be quantitatively estimated.

4.5. Histological and serum analysis

All model animals were sacrificed on the third day following the completion of modeling injections at weeks 1, 2, 3, 4, 6, 8, 12, and 16 ($n \geqslant 5$ per time point). Blood and liver tissue samples were subsequently collected. Anticoagulated blood was left to stand at room temperature for 2 h, followed by centrifugation at 4 °C, 3000 rpm, for 10 min to obtain the supernatant. The supernatant was labeled and stored temporarily at −80 °C. After two days of freezing, the samples were sent to a testing laboratory (Wuhan Servicebio Technology Co., Ltd) for the measurement of ALT and AST levels, which are both important biomarkers for assessing liver function and detecting liver injury.

The freshly excised liver tissues were washed with saline to remove any residual blood, weighed, and photographed. They were then divided into two groups. The first group was placed in a MACS tissue storage solution (Miltenyi, Order No.: 130–100–008) and temporarily stored in an ice box. Subsequently, the liver tissues were sliced into 300 μm thick sections using a vibrating blade microtome (Leica Biosystems, VT1000 S, with a blade travel speed setting of 0.05 mm s^{-1}, vibration frequency of 70 Hz and positioning resolution < 1 μm). The freshly cut liver sections were immediately placed under a PAEM device for scanning and data collection to ensure the liver's stiffness remained consistent with its physiological state. The other group was placed in a container filled with 4% paraformaldehyde fixation solution and stored at

4 °C for preservation. Once all liver tissues from the animals (1–16 weeks models) were collected, they were sent to a biological services company (Wuhan Servicebio Technology Co., Ltd) for HE staining, Masson staining, and scanning, ensuring consistency in the staining background.

4.6. Data processing and statistics

SWE examinations and LSM values were obtained from the system-installed software. All PA data was processed with algorithms developed by us based on MATLAB. PA images were reconstructed as MIP maps and ToFs were calculated with mean maximum peak of PA signals. In structural analysis, low-absorption regions corresponding to collagen fiber crevices were extracted from the PA image via thresholding to generate a binary mask. Using distance transform-derived watershed seed points, a gradient-modified watershed algorithm segmented these regions as irregularly shaped pseudo-lobules. Randomized color coding was applied to adjacent regions to prevent chromatic ambiguity. Pseudo-lobular features were subsequently quantified via area-equivalent diameter measurements. In stiffness measurements, ΔToF was calculated with the formula $|\mathrm{ToF}_{\mathrm{background}}—\mathrm{ToF}_{\mathrm{liver}}|$, where six ROIs of $500 * 500\ \mu$m were randomly selected in each sample (three for background and three for liver). In each group, there were 11–25 samples used for calculation of mean values and their standard error. ΔToF values analyses were performed with Shapiro–Wilk test, and the comparisons between groups were based on a one-way ANOVA procedure in OriginPro 2022. Incorporating leave-one-out cross-validation in ROC curve analysis for AUC computation significantly enhances the robustness of diagnostic model performance evaluation. Some icons in the schematic were from BioRender. All curves were produced using OriginPro 2022.

Data availability statement

All data that support the findings of this study are included within the article (and any supplementary files).

Supplementary data available at https://doi.org/10.1088/2515-7647/ae0541/data1.

Acknowledgments

We acknowledge the supporting of the National Natural Science Foundation of China (NSFC) (81930048, 82330061, 82372010), National Key R&D Program of China (2023YFF0715303), Guangdong Science and Technology Commission (2019BT02X105), Hong Kong Research Grant Council (15217721, 15125724, C7074-21GF), Hong Kong Polytechnic University (P0038180, P0039517, P0043485, P0045762, P0049101), College of Professional and Continuing Education Research Fund (SEHS-2023-308(I)), and Faculty Development Scheme (UGC/FDS24/M02/24). During the manuscript revision phase, AI-assisted tools (ChatGPT, DeepSeek) were employed to enhance the linguistic refinement of the text.

Conflict of interest

The authors declare no conflict of interest.

Author contributions

Weiran Pang 0000-0002-7685-2344
Conceptualization (lead), Data curation (lead), Formal analysis (lead), Methodology (equal), Software (equal), Validation (equal), Visualization (lead), Writing – original draft (lead), Writing – review & editing (equal)

Qi Zhou
Data curation (supporting), Formal analysis (supporting), Investigation (supporting), Resources (equal), Writing – review & editing (supporting)

Yang Qiu
Software (equal), Validation (supporting), Visualization (supporting), Writing – review & editing (supporting)

Haofan Huang
Methodology (supporting), Software (supporting), Validation (supporting), Writing – review & editing (supporting)

Jiali Chen
Data curation (supporting), Formal analysis (supporting), Investigation (supporting), Writing – review & editing (supporting)

Tianting Zhong
Methodology (supporting), Visualization (supporting), Writing – review & editing (supporting)

Yingying Zhou 0000-0002-9313-6825
Conceptualization (equal), Investigation (equal), Methodology (equal), Resources (equal), Writing – review & editing (supporting)

Liming Nie 0000-0002-1781-4612
Conceptualization (supporting), Project administration (equal), Supervision (equal), Writing – review & editing (equal)

Puxiang Lai 0000-0003-4811-2012
Conceptualization (equal), Methodology (equal), Project administration (lead), Resources (equal), Supervision (lead), Writing – review & editing (equal)

References

[1] Insana M F and Bamber J C 2000 Tissue motion and elasticity imaging *Phys. Med. Biol.* **45** 001
[2] Joshi R, Singh A, Jajoo N, Pai M and Kalantri S P 2004 Accuracy and reliability of palpation and percussion for detecting hepatomegaly: a rural hospital-based study *Indian J. Gastroenterol.* **23** 171–4
[3] Ghany M G and Doo E 2005 Assessment of liver fibrosis: palpate, poke or pulse? *Hepatology* **42** 759–61
[4] Park C C *et al* 2017 Magnetic resonance elastography vs transient elastography in detection of fibrosis and noninvasive measurement of steatosis in patients with biopsy-proven nonalcoholic fatty liver disease *Gastroenterology* **152** 598–607.e2
[5] Zhou M *et al* 2025 Multi-scale spatial heterogeneity of liver fibrosis evaluated by MR elastography in rat models *J. Magn. Resonan. Imaging* 1–13
[6] Wilson M P, Singh R, Mehta S, Murad M H, Fung C and Low G 2025 Comparing FIB-4, VCTE, pSWE, 2D-SWE, and MRE thresholds and diagnostic accuracies for detecting hepatic fibrosis in patients with MASLD: a systematic review and meta-analysis *Diagnostics* **15** 1598
[7] Sigrist R M S, Liau J, Kaffas A E, Chammas M C and Willmann J K 2017 Ultrasound elastography: review of techniques and clinical applications *Theranostics* **7** 1303
[8] Zvietcovich F, Pongchalee P, Meemon P, Rolland J P and Parker K J 2019 Reverberant 3D optical coherence elastography maps the elasticity of individual corneal layers *Nat. Commun.* **10** 4895
[9] Feng X, Li G-Y, Ramier A, Eltony A M and Yun S-H 2022 In vivo stiffness measurement of epidermis, dermis, and hypodermis using broadband Rayleigh-wave optical coherence elastography *Acta Biomater.* **146** 295–305
[10] Rippy J R, Singh M, Aglyamov S R and Larin K V 2021 Ultrasound shear wave elastography and transient optical coherence elastography: side-by-side comparison of repeatability and accuracy *IEEE Open J. Eng. Med. Biol.* **2** 179–86
[11] Singh M, Hepburn M S, Kennedy B F and Larin K V 2025 Optical coherence elastography *Nat. Rev. Methods Primers* **5** 39
[12] Li M, Liu L, Xi N and Wang Y 2018 Atomic force microscopy studies on cellular elastic and viscoelastic properties *Sci. China Life Sci.* **61** 57–67
[13] Bataller R and Brenner D A 2005 Liver fibrosis *J. Clin. Invest.* **115** 209–18
[14] Dietrich C F *et al* 2017 EFSUMB guidelines and recommendations on the clinical use of liver ultrasound elastography, update 2017 (long version) *Ultraschall in der Medizin-European J. Ultrasound* **38** e16–e47
[15] Martinez S M, Crespo G, Navasa M and Forns X 2011 Noninvasive assessment of liver fibrosis *Hepatology* **53** 325–35
[16] Poynard T *et al* 2013 Liver fibrosis evaluation using real-time shear wave elastography: applicability and diagnostic performance using methods without a gold standard *J. Hepatol.* **58** 928–35
[17] Wang L V 2009 Multiscale photoacoustic microscopy and computed tomography *Nat. Photon.* **3** 503–9
[18] Ruiz-Veloz M, Gutiérrez-Juárez G, Polo-Parada L, Cortalezzi F, Kline D D, Dantzler H A, Cruz-Alvarez L, Castro-Beltrán R and Hidalgo-Valadez C 2023 Image reconstruction algorithm for laser-induced ultrasonic imaging: the single sensor scanning synthetic aperture focusing technique *J. Acoust. Soc. Am.* **153** 560
[19] Pang W *et al* 2024 Direct monitoring of whole-brain electrodynamics via high-spatiotemporal-resolution photoacoustics with voltage-sensitive dye *Laser Photonics Rev.* **18** 2400165
[20] Singh M S and Thomas A 2019 Photoacoustic elastography imaging: a review *J. Biomed. Opt.* **24** 040902
[21] Hai P, Zhou Y, Gong L and Wang L V 2016 Quantitative photoacoustic elastography in humans *J. Biomed. Opt.* **21** 066011
[22] Wan M, Zhang Y, Li J, Qian Z, Gao F, Yang Y and Li W 2024 Optical-resolution photoacoustic microelastography system for elasticity mapping: phantom study and practical application *J. Biophoton.* **17** e202400032
[23] Hu P, Zhao P, Qu Y, Maslov K, Chubiz J, Tuuli M G, Stout M J and Wang L V 2024 Quantification of cervical elasticity during pregnancy based on transvaginal ultrasound imaging and stress measurement *IEEE Trans. Biomed. Eng.* **71** 2948–55
[24] Yang F, Chen Z, Wang P and Shi Y 2024 Phase-domain photoacoustic mechanical imaging for quantitative elastography and viscography *IEEE Trans. Biomed. Eng.* **71** 2330–40
[25] Mandal S *et al* 2019 Determining elastic contrast in tissue-mimicking phantoms using frequency resolved photoacoustic imaging *Proc. SPIE* **10878** 108782M
[26] Yuan Y, Wen X, Yuan B, Xin H, Fang B, Yang S and Xiong K 2023 Photoacoustic remote sensing elastography *Opt. Lett.* **48** 2321–4
[27] Cai C, Wang X, Si K, Qian J, Luo J and Ma C 2019 Feature coupling photoacoustic computed tomography for joint reconstruction of initial pressure and sound speed in vivo *Biomed. Opt. Express* **10** 3447–62
[28] Hai P, Yao J, Li G, Li C and Wang L V 2016 Photoacoustic elastography *Opt. Lett.* **41** 725–8

[29] Li W *et al* 2025 Quantification of vascular remodeling and sinusoidal capillarization to assess liver fibrosis with photoacoustic imaging *Radiology* **314** e241275

[30] Qiu Y, Li H, Yu K, Chen J, Qi L, Zhao Y and Nie L 2025 Collagen fibers quantification for liver fibrosis assessment using linear dichroism photoacoustic microscopy *Photoacoustics* **42** 100694

[31] Carrillo F, Gupta S, Balooch M, Marshall S J, Marshall G W, Pruitt L and Puttlitz C M 2005 Nanoindentation of polydimethylsiloxane elastomers: effect of crosslinking, work of adhesion, and fluid environment on elastic modulus *J. Mater. Res.* **20** 2820–30

[32] Kondo S and Igarashi T 1980 Hypersonic sound velocity in liquid and rubbery polymers *J. Appl. Phys.* **51** 1514–9

[33] Ormachea J and Parker K J 2022 A preliminary study of liver fat quantification using reported ultrasound speed of sound and attenuation parameters *Ultrasound Med. Biol.* **48** 675–84

[34] Yu Z *et al* 2022 Wavefront shaping: a versatile tool to conquer multiple scattering in multidisciplinary fields *Innovation* **3** 100292

[35] Cheng S, Zhou Y, Chen J, Li H, Wang L and Lai P 2022 High-resolution photoacoustic microscopy with deep penetration through learning *Photoacoustics* **25** 100314

[36] Huang T *et al* 2023 Artificial intelligence for medicine: progress, challenges, and perspectives *Innov. Med.* **1** 100030

[37] Zhou Y, Chen J, Liu C, Liu C, Lai P and Wang L 2019 Single-shot linear dichroism optical-resolution photoacoustic microscopy *Photoacoustics* **16** 100148